Draft version 2017/04/26
Preprint typeset using LaTeX style emulateapj v. 11/10/09

A CATALOG OF 3MM POINT SOURCES IN THE SGR B2 CLOUD: SIGNS OF EXTENDED STAR FORMATION IN A CMZ CLOUD

Adam Ginsburg[1],

[1] *National Radio Astronomy Observatory, Socorro, NM 87801 USA*
aginsbur@nrao.edu

Draft version 2017/04/26

ABSTRACT

We report the detection of > 100 sources in the Sgr B2 clouds with extents smaller than 5000 AU. These sources are most likely to be protostars or centrally condensed prestellar cores. The spatial distribution of these sources demonstrates that Sgr B2 is experiencing a highly extended star formation event, not just an isolated 'starburst' within the protocluster regions M, N, and S.

1. INTRODUCTION

The Central Molecular Zone (CMZ) of our Galaxy appears to be overall deficient in star formation relative to the gas mass it contains (Longmore et al. 2013; Kauffmann et al. 2016a,b; Barnes et al. 2016, 2017). This deficiency suggests that star formation laws, i.e., the empirical relations between the star formation rate and gas density, are not universal. The gas conditions in the Galactic center provide a powerful lever-arm in a few parameters (e.g., pressure, temperature, velocity dispersion Ginsburg et al. 2016; Immer et al. 2016; Shetty et al. 2012; Henshaw et al. 2016) to assess the influence of environmental effects on star formation.

The observations that have demonstrated the star formation deficiency compare bulk tracers of star formation to $\gtrsim 0.1$ pc resolution gas observations (Barnes et al. 2017, e.g.). More recently, high-resolution observations of selected clouds in the CMZ have revealed very few star-forming cores even when examined at high resolution and sensitivity (Rathborne et al. 2015; Kauffmann et al. 2016a,b). The only sites with obvious signs of ongoing star formation along the CMZ dust ridge are the Sgr B2 N, M, and S protoclusters (Schmiedeke et al. 2016) and, at a much lower level, Clouds C, D, and E (Ginsburg et al. 2015, Walker et al, in prep; Barnes et al, in prep). These regions contain a handful of high-mass cores detected with ALMA, but only a small number of protostars.

We report the first observations of extended, ongoing star formation in a Galactic center cloud *not* isolated to a centralized protocluster dust clump. We observed the entire Sgr B2 cloud and identified star formation along the entire molecular dust ridge known as Sgr B2 Deep South (DS). These observations allow us to perform the first star-counting based determination of the star formation rate within the molecular gas of the CMZ.

We describe the observations in Section 2. In this paper, we focus on the continuum sources, which we identify in Section 3.1. We classify the sources in Section 4.1.

2. OBSERVATION AND DATA REDUCTION

Data were acquired as part of ALMA project 2013.1.00269.S. Observations were taken with the 12m Total Power array, the ALMA 7m array, and in two configurations with the ALMA 12m array. The setup included the maximum allowed number of channels, 30720, across 4 spectral windows in a single polarization; the single-polarization mode was adopted to support moderate spectral resolution across the broad bandwidth.

The ALMA QA2 calibrated measurement sets were combined to make a single high-resolution, high-dynamic range data set. We imaged the continuum jointly across all four bands, and found that the central regions surrounding Sgr B2M were severely affected by artifacts that could not be cleaned out. We therefore ran 3 iterations of phase-only self-calibration and one iteration of amplitude + phase self-calibration to yield a substantially improved image. The total dynamic range, measured as the peak brightness in Sgr B2 to the RMS noise in a signal-free region of the image, is 22000 (noise ~ 0.08 mJy/beam), while the dynamic range within one primary beam ($\sim 0.5'$) of Sgr B2M is only 3700 (noise ~ 0.5 mJy/beam). Because of the dynamic range limitations, and an empirical determination that clean did not converge if allowed to go too deep, we cleaned to a threshold of 0.5 mJy/beam across the image. We performed this same process for both the longest-baseline data only (resolution $\sim 0.5''$, largest angular scale theoretically $15''$ [the shortest baseline] but more practically $\sim 7''$ [the 5th percentile baseline length]) and the merged 7m + two 12m configuration data. The merged data are more useful for studying extended structures but have lower dynamic range, while the long-baseline-only data are excellent for extracting and analyzing pointlike or compact sources.

We also produced cubes of all of the spectral lines. These were lightly cleaned with only 200 iterations of cleaning. No self-calibration was applied. Before continuum subtraction, dynamic range related artifacts similar to those in the continuum images were present, but these structures are identical across frequencies, and were therefore removable in the image domain. We use median-subtracted cubes for the majority of our analysis, noting that the only location in which an error on the continuum $> 5\%$ is expected is the Sgr B2 North core (Sanchez-Monge et al. 2017).

3. ANALYSIS

3.1. *Continuum Source Identification*

We selected continuum point sources as candidate cores or protostars by eye. An automated selection is not viable across the majority of the field because there are many extended H II regions that dominate the overall map emission. A future automated selection algorithm may work if images at comparable resolution at other frequencies become available; the H II-region sources could then be excluded. Additionally, however, there are substantial imaging artifacts produced by the extremely bright emission sources in Sgr B2 M ($S_{3mm,max} > 0.8$ Jy) and Sgr B2 N ($S_{3mm,max} > 0.3$ Jy) that make automated source identification particularly challenging in the most source-dense regions.

Because the noise varies significantly across the map, a uniform selection criterion is not possible. We therefore include two levels of source identification, 'high confidence' sources, which are selected conservatively in regions of low-background, and 'low-confidence' sources that are somewhat lower signal-to-noise and are often in regions with higher background. Both of these selection criteria are significantly more conservative than a local $5-\sigma$ threshold.

We measure the local noise for each source by taking the median absolute deviation in an annulus 0.5 to 1.5 $''$ around the source center. All but 7 sources have signal-to-local-noise ratios $S/N > 7$. These sources are all in regions of particularly high background or source density and therefore have overestimated local noise.

Our selection criteria result in a reliable but potentially incomplete catalog.

4. RESULTS

We detected 138 compact continuum sources. Their flux distribution is shown in Figure 7.

4.1. *Source Classification*

For the majority of the detected sources, we have only a continuum detection at 3 mm. No lines are detected peaking toward most of the sources, especially the faint ones. A subset have detections at other bands and can be classified based on previous literature work, especially those associated with H II regions detected at 0.7 and 1.3 cm (Gaume et al. 1995; Mehringer et al. 1995; de Pree et al. 1996; Pree et al. 2015). In this section, we employ various means to classify the sample of new sources.

We first note some key properties of dust at 3 mm. At 8.4 kpc, a 1 mJy source corresponds to an optically thin dust mass of $M(40\mathrm{K}) = 18\ M_\odot$ or $M(20\mathrm{K}) = 38\ M_\odot$ assuming a dust opacity index $\beta = 1.75$ to extrapolate the Ossenkopf & Henning (1994) opacity to $\kappa_{3mm} = 0.0018$ cm^2 g^{-1}. Our dust-only 5-σ sensitivity limit at 40 K therefore ranges from $M > 7\ M_\odot$ (0.5 mJy) to $M > 45$ $M_\odot$ (2.5 mJy) across the map. If we were to assume that these are all cold, dusty sources, as is typically (and reasonably) assumed for local clouds, they would be extremely massive and dense, with the lowest measurable density being $n(40\mathrm{K}) > 3\times10^6$ cm^{-3} (corresponding to 7 $M_\odot$ in a $0.5''$ radius sphere). Such extreme objects are possible, but since we have detected > 100 of these sources, it makes sense to evaluate other possibilities.

4.1.1. *Alternative 1: The sources are externally ionized gas blobs*

One possibility is that these sources are not dusty at all, nor pre- or protostellar, but are instead the brightest compact clumps surrounding H II regions. They would then be analogous to the heads of cometary clouds, externally ionized globules ("EGGs"), or proplyds, and their observed emission would give no clue to their nature because the light source is extrinsic.

The majority of the detected sources have size $<$ 4000 AU, i.e., they are unresolved. By contrast, the free-floating EGGs so far observed have sizes 10,000-20,000 AU (Sahai et al. 2012a,b), so they would be resolved in our observations. Toward the brightest frEGG in Cygnus X, Sahai et al. (2012b) measured a peak intensity $S_{8.5GHz} \approx 1.5$ mJy/beam in a $\approx 3''$ beam. Cygnus X is 6$\times$ closer that the Galactic center, so their beam size is the same physical scale as ours. If the free-free emission is thin, the brightness in our data would be $S_{95GHz} = (95/8.5)^{-0.1} S_{8.5GHz} = 0.79 S_{8.5GHz} \approx 1.2$ mJy/beam. These frEGGs would be detectable in our data. Comparison to radio observations at a comparable resolution will be needed to rule out the externally ionized globule hypothesis for resolved regions.

If the detected sources were either EGGs or cometary clouds, we would expect them to be located within H II regions. Many of the sources are near H II regions, as seen in Figure 2. However, they are nearly all associated with a ridge of HC_3N emission (Figure 3). If they are deeply embedded within the molecular material, they cannot be externally ionized. The current data do not provide enough information on the geometry of the clouds to rule out the possibility that the point sources are just illuminated cloud edges, but the fact that the ionized gas is brightest adjacent to, rather than on top of, the HC_3N suggests that the HC_3N traces a full molecular cloud rather than a thin PDR-like layer.

4.1.2. *Alternative 2: The sources are* H II *regions produced by interloper ionizing stars*

If there is a large population of older, but still ionizing, stars, they could ignite H II regions when they fly through molecular material. See 4.1.3 for calculations of stationary H II region properties. The main problem with this scenario is the spatial distribution of the observed sources. While most of the continuum sources are associated with dense gas and dust ridges, not all of the high-column molecular gas regions have such sources in them (i.e., the left and right sides of the image in Figure 3, where molecular material is seen with no associated millimeter sources). If there is a free-floating population of OB stars responsible for the 3 mm point source population, their distribution should match that of the gas. Also, there is no such population of sources seen outside of the dense gas in the infrared (TODO: Who has done infrared studies of Sgr B2? You can infer what I have stated 'by inspection' of 2MASS, but it would be more straightforward to quote someone else), which again we should expect if there is a uniformly distributed population.

4.1.3. *Alternative 3: The sources are* H II *regions produced by recently-formed OB stars*

For an unresolved spherically symmetric H II region ($R = 4000$ AU), the expected flux density is $S_{95\mathrm{GHz}} = 4.7$ mJy for a $Q_{lyc} = 10^{47}$ s^{-1} source (assuming $T_e = 7000$

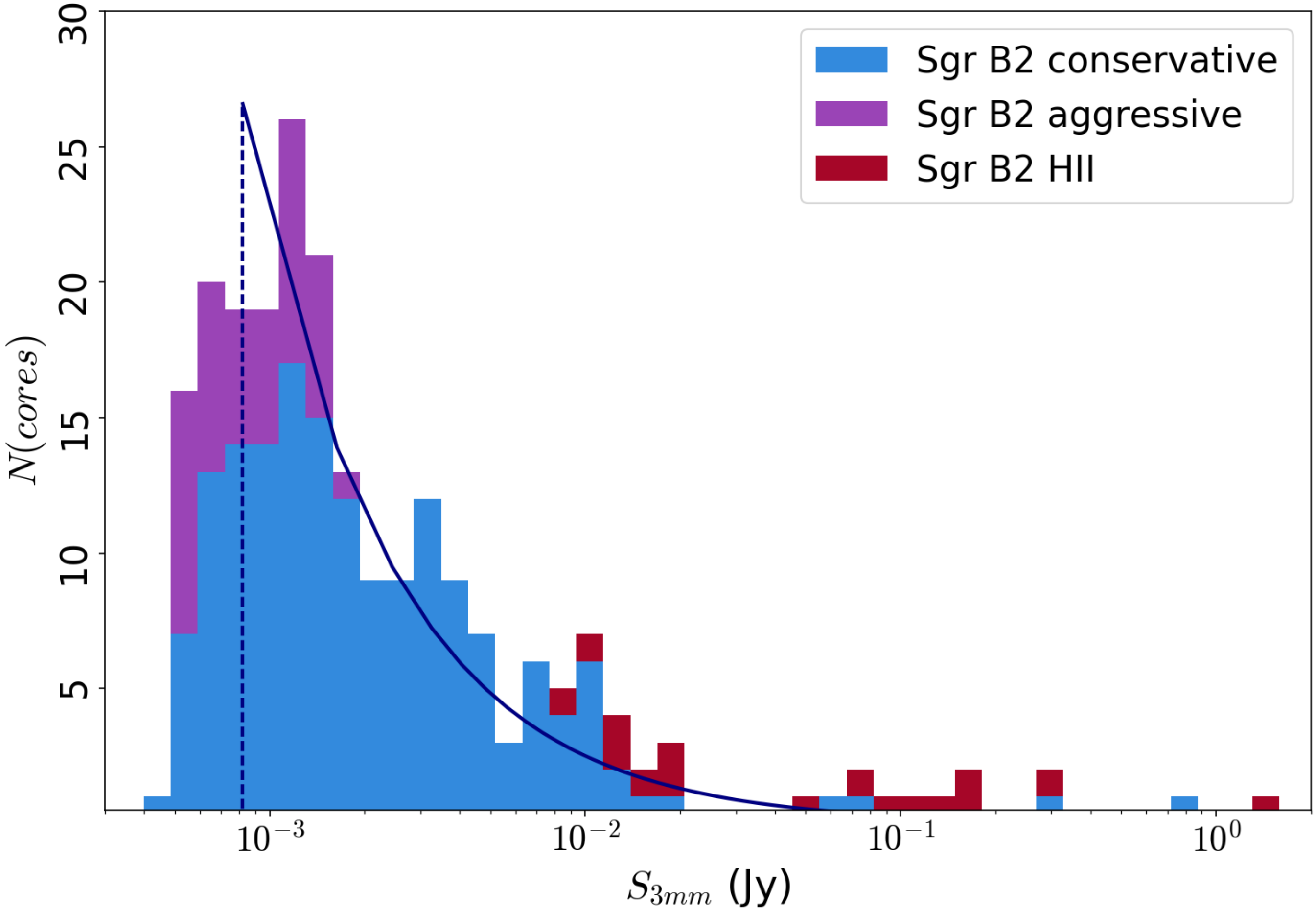

FIG. 1.— A histogram of the peak flux density of the observed sources excluding known H II regions with a powerlaw fit shown. The fitted powerlaw is an excellent fit to the data, but is far shallower than the IMF slope, with $\alpha = 1.94 \pm 0.07$. The two brightest regions are Sgr B2M f1 and Sgr B2N K2, which may be dominated by free-free emission but likely also contain a large dust mass.

K), and that value scales linearly with Q_{lyc} as long as the source is optically thin. Rearranging Condon & Ransom (2007) equations 4.60 and 4.61:

$$\begin{aligned} S_\nu(Q_{lyc}) &= 4.67 \left[1 - \exp\left(c_* T_* \nu_* EM_*\right)\right] \\ \nu_* &= \left(\frac{\nu}{\mathrm{GHz}}\right)^{-2.1} \\ T_* &= \left(\frac{T_e}{10^4\mathrm{K}}\right)^{-1.35} \\ c_* &= -3.28 \times 10^{-7} \\ EM_* &= \frac{3Q_{lyc}}{4\pi R^2 \alpha_b} \end{aligned} \tag{1}$$

where $\alpha_b = 2 \times 10^{-13}$ cm^3 s^{-1}, Q_{lyc} is the count rate of ionizing photons in s^{-1}, and R is the H II region radius.

An extremely compact H II region, e.g., one with $R <$ 100 AU and corresponding density $n > 10^6$ cm^{-3}, would be optically thick and therefore fainter, $S_{95\mathrm{GHz}}(R = 100\mathrm{AU}, Q_{lyc} = 10^{47}\mathrm{s}^{-1}) = 3.4$ mJy. Even the brightest O-stars could produce H II regions as faint as 0.5 mJy if embedded in extremely high density gas; above $Q_{lyc} > 10^{47}$ s^{-1}, a 25 AU H II region would be ~ 0.5 mJy.

Figure 4 shows the predicted brightness for various H II regions produced by OB stars and the density required for those H II regions to be the specified size. In order for the detected sources to be O-star-driven H II regions, with $10^{47} < Q_{lyc} < 10^{50}$ s^{-1}, they must be optically thick and therefore extremely compact and dense. There is a narrow range of late O/early B stars, $10^{46} < Q_{lyc} < 10^{47}$ s^{-1}, that could be embedded in compact H II regions of almost any size and produce the observed range of flux densities. Anything fainter, later than $\sim$B0 ($Q_{lyc} < 10^{46}$ s^{-1}), would be incapable of producing the observed flux densities. Any brighter stars would have to be embedded in dust that, at 40 K, would outshine the H II region; more likely, such sources would have much hotter dust and therefore would be much brighter (and more extended) than our observations allow.

This restrictive parameter space, combined with a steep luminosity function that implies there are many more sources at slightly lower luminosity, is evidence against the population being dominated by H II regions.

4.1.4. *The sources are protostars*

After ruling out the other hypotheses, we conclude that these sources are predominantly embedded protostars. Their emission is likely dust-dominated, but is probably warmer than the cloud average $\sim 20-40$ K. We test and

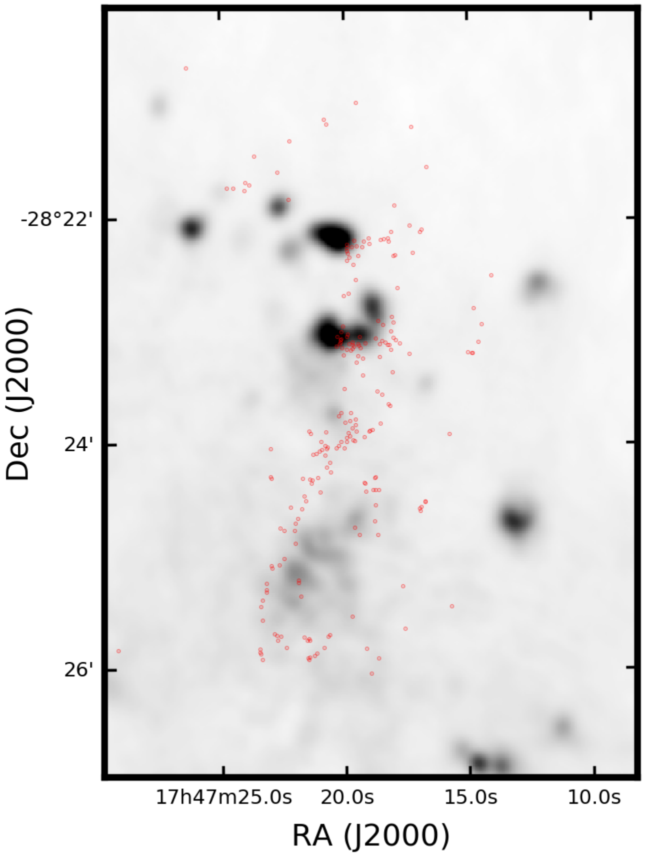

FIG. 2.— The location of the detected continuum sources (red points) overlaid on a 20 cm continuum VLA map highlighting the diffuse free-free (or possibly synchrotron) emission in the region (Yusef-Zadeh et al. 2004).

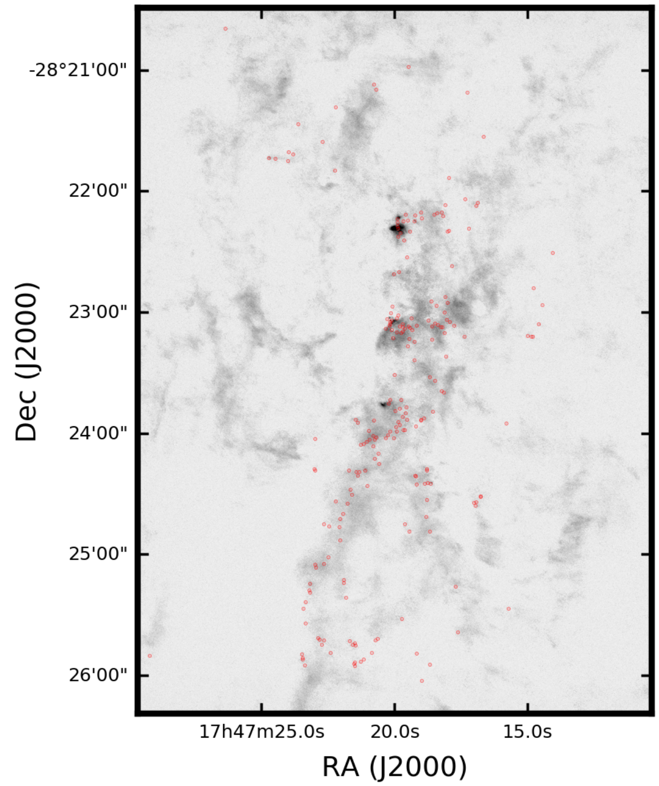

FIG. 3.— The location of the detected continuum sources (red points) overlaid on a map of the HC_3N peak intensity. HC_3N traces moderate-density molecular gas.

validate the hypothesis that most or all of the sources are protostellar in this section.

We cross-matched out source catalog with catalogs of H II regions and methanol masers. Class II methanol masers are always associated with sites of high-mass star formation. The Caswell et al. (2010) Methanol Multi-beam Survey identified 11 sources in our observed field of view, of which 10 have a clear match in our catalog. Several other sources in our catalog match known H II regions from Gaume et al. (1995), mostly associated with the brightest sources in our sample; these all have $S_{3\mathrm{mm}} > 9$ mJy.

We compare our detected sample to that of the Herschel Orion Protostar Survey (HOPS; Furlan et al. 2016) in order to get a general sense of what types of sources we have detected. We selected this survey for comparison because it is one of the largest protostellar core samples with well-characterized bolometric luminosities available. Figure 5 shows the HOPS source fluxes at 870μm scaled to 3 mm assuming a dust opacity index $\beta = 1.5$, which is shallower than usually inferred, so the extrapolated fluxes may be slightly overestimated. The 870μm data were acquired with a $\sim 20''$ FWHM beam, which translates to a resolution $\sim 1''$ at $d_{SgrB2} = 8.4$ kpc assuming $d_{Orion} = 415$ pc, so our beam size is somewhat smaller than theirs. The HOPS sources are all fainter than the Sgr B2 sources. The brightest HOPS source, with $L_{tot} < 2000\ L_\odot$, would only be 0.2 mJy in Sgr B2, or about a 4-σ source - below our detection threshold even in the noise-free regions of the map. We conclude that the Sgr B2 sources are much more luminous and are therefore massive protostars.

This conclusion is supported by a more direct comparison with the Orion nebula as observed at 3 mm with MUSTANG (Dicker et al. 2009, Figure 6). Their data were taken at $9''$ FWHM resolution, corresponding to $0.48''$ at d_{SgrB2}. The peak flux density measured in that map is toward Source I, $S_{90GHz}(d_{SgrB2}) = 3.6$ mJy. Source I would therefore be detected and would be somewhere in the middle of our sample. It is extended, and the extended component would be readily detected in our data. Since Source I is the only known high-mass YSO in the Orion cloud, and it would be detectable while no other sources in the Orion cloud would be, it appears safe to conclude that all of our detected sources are MYSOs.

The flux density distribution of the non-H II region sources follows a powerlaw with slope $\alpha = 1.94 \pm 0.07$ (fitted with the MLE method of Clauset et al. 2007). If we assume that the stellar mass is linearly proportional to the 3 mm continuum flux density, this measurement implies a slope shallower than the $\alpha \sim 2.35$ expected for a normal IMF. It is possible that the IMF is genuinely different from Salpeter here, but it is more likely that the more massive stars are surrounded by warmer gas, implying that the source mass distribution is steeper than the source flux distribution.

If we make the very simplistic assumptions that the sources we detect are all $L \gtrsim 2000\ L_\odot$ ($M \gtrsim 8 M_\odot$),

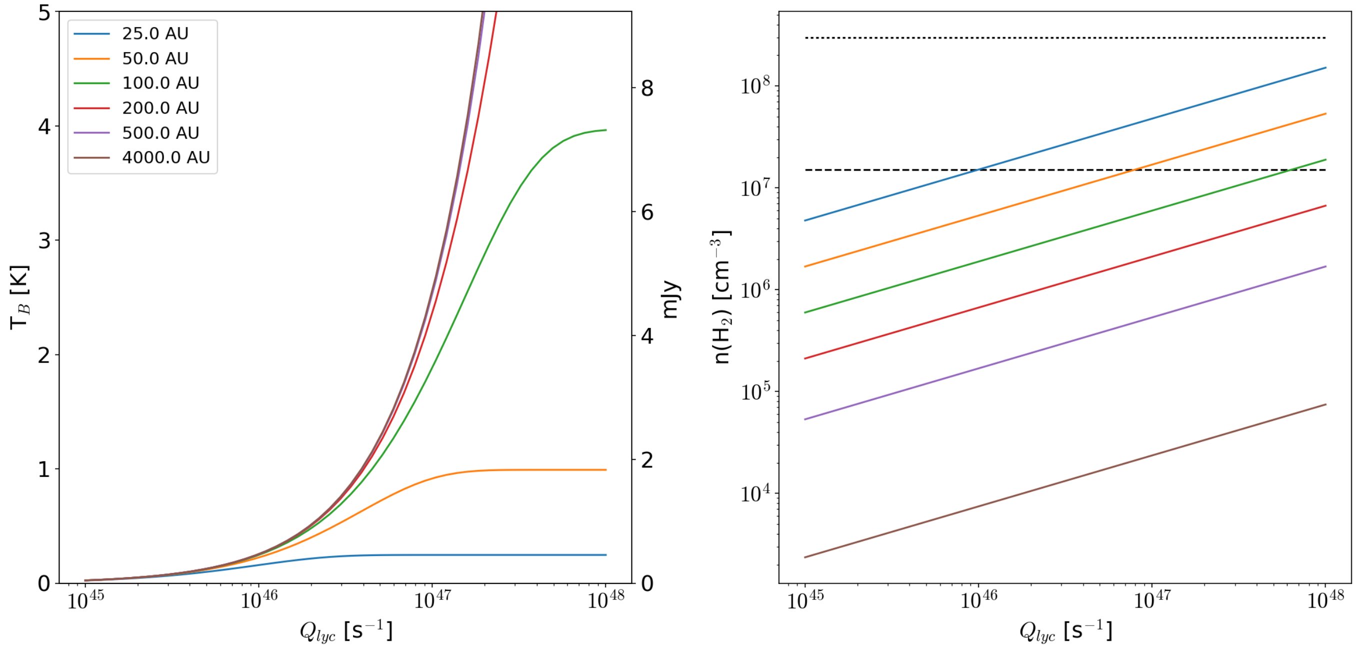

FIG. 4.— Simple models of spherical H II regions to illustrate the observable properties of such regions. The H II region size is shown by line color; the legend in the left plot applies to both figures. (left) The expected brightness temperature (left axis) and corresponding flux density within a FWHM=0.5″ beam (right axis) as a function of the Lyman continuum luminosity for a variety of source radii. (right) The density required to produce an H II region of that radius. The horizontal dashed line shows the density corresponding to an unresolved dust source at the 5-σ detection limit ($\approx$ 0.5 mJy, or about 10 $M_\odot$ of dust, assuming $T = 40$ K). Above this line, dust emission would dominate over free-free emission. The dotted line shows the density required for dust emission to produce a 10 mJy source at $T = 40$ K. As seen in the left plot, for any moderate-sized H II region, $R > 100$ AU, a high-luminosity star ($Q_{lyc} > 10^{47}$ s^{-1}) would produce an H II region brighter than the majority of our sample, which includes only a few sources brighter than 10 mJy. The densities required to produce H II regions within our observed range ($1 < S_\nu < 10$ mJy) are fairly extreme, $n \gtrsim 10^6$ cm^{-3}, for O-stars.

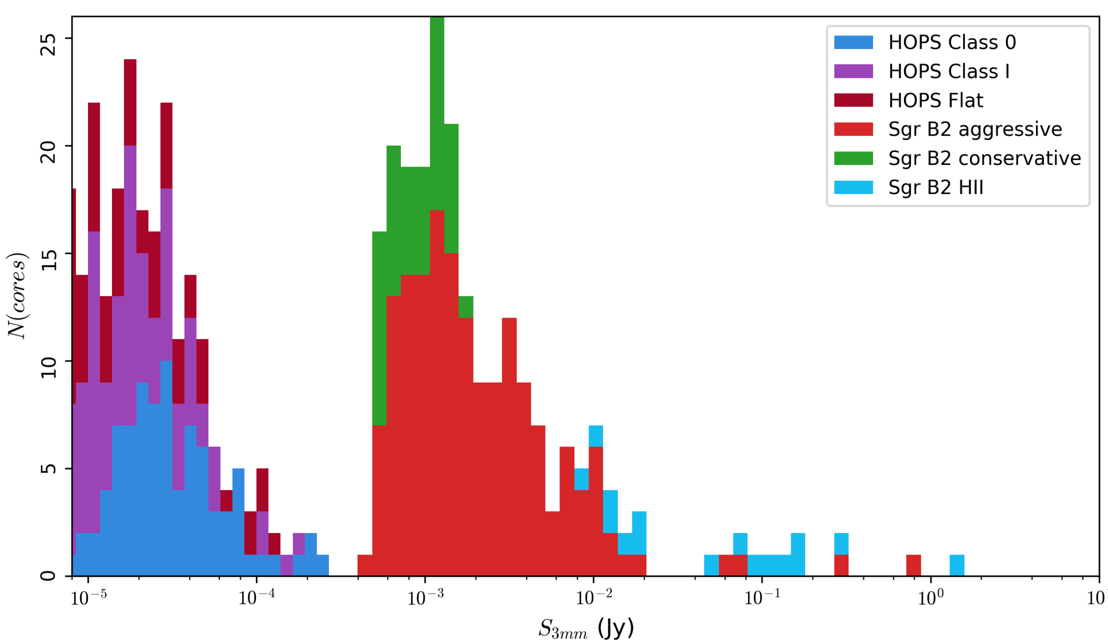

FIG. 5.— A histogram combining the detected Sgr B2 cores with predicted flux densities based on the HOPS (Furlan et al. 2016) survey. The HOPS histogram shows the 870 μm data from that survey scaled to 3 mm assuming $\beta = 1.5$. Every HOPS source is well below the detection threshold for our observations.

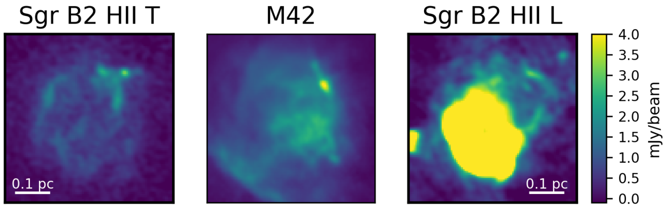

FIG. 6.— Comparison of two extended H II regions in Sgr B2 to the M42 nebula in Orion. The three panels are shown on the same physical and color scale assuming $d_{Orion} = 415$ pc and $d_{SgrB2} = 7.8$ kpc and that the ALMA and MUSTANG data have the same continuum bandpass. Sgr B2 H II T is comparable in brightness and extent to M42; Sgr B2 H II L is much brighter and is saturated on the displayed brightness scale. The compact source to the top right of the M42 image is Orion Source I; the images demonstrate that Source I and the entire M42 nebula would be easily detected in our data.

we can infer the total (proto)stellar mass in the observed region. Using a Kroupa (2001) mass function with $M_{max} = 200\ M_\odot$, 23% of the mass is contained in $M > 8 M_\odot$ stars. Using $M = 8 M_\odot$ as the lower-limit case for each source, the identified sources have total mass $M(>8) = 1800 M_\odot$. The total stellar mass implied is $M_{tot} = 8 \times 10^3\ M_\odot$. If instead we use the mean stellar mass for $M > 8\ M_\odot$, $\bar{M} = 21.1\ M_\odot$, then $M_{tot} = 2 \times 10^4\ M_\odot$. These are lower limits in the Sgr B2 N and M regions because our catalog is incomplete due to confusion and dynamic range limitations. Additionally, we are using a single-star IMF and our resolution is only ~ 4000 AU, so it is likely that we have undercounted by $\gtrsim 2\times$, since high-mass stars have a high multiplicity fraction (Mason et al. 2009).

We compare our mass estimates to those of Schmiedeke et al. (2016), who inferred stellar masses primarily from H II region counts.

- Cluster M : N(cores)= 10 N(HII)= 13 counted mass= 711.30 inferred mass= 5600.08
- Cluster N : N(cores)= 10 N(HII)= 2 counted mass= 210.70 inferred mass= 2007.45
- Cluster NE: N(cores)= 4 N(HII)= 0 counted mass= 47.87 inferred mass= 541.70
- Cluster S : N(cores)= 3 N(HII)= 0 counted mass= 35.91 inferred mass= 406.27

4.2. *An examination of star formation thresholds*

4.2.1. *Comparison to other CMZ clouds*

Lada et al, and others, have proposed that star formation can only occur above a certain density or column density threshold[1]. In G0.253+0.016, very little star formation has been observed (Longmore et al. 2013; Johnston et al. 2014; Rathborne et al. 2015) despite most of the cloud existing above the locally measured column density threshold.

Since we have detected substantial ongoing star formation in the form of high-mass protostars and/or protostellar cores, we can assess where these stars form and whether the same (lack of) a threshold exists in Sgr B2. We therefore plot the column density distribution (flux distribution?) and overlay the cumulative distribution function of the background brightness around the cores.

[1] Column density is more commonly used because of its observational convenience, but it is physically meaningless unless high column density leads to high optical depths and thereby changes the gas's ability to cool.

Comparing Sgr B2 to G0.253, the majority of the Sgr B2 cloud is brighter and at higher column than G0.253. The presence of star formation in Sgr B2 nearly all occurs at a higher column than exists within G0.253 (Figure 7). The lack of SF in the brick is therefore consistent with the active SF in Sgr B2 and the CMZ's higher SF threshold is confirmed.

4.2.2. *Comparison to Lada, Lombardi, and Alves 2010*

In this section, we compare the star formation threshold in Sgr B2 to that in local clouds performed by Lada et al. (2010). They determined that all star formation in local clouds occurs above a column density threshold $M_{thresh} > 116\ M_\odot$ pc^{-2}, or $N_{thresh}(H_2) > 5.2 \times 10^{21}$ cm^{-2} assuming the mean particle mass is 2.8 amu (Kauffmann et al. 2008). We first note, then, that *all pixels* in our column density maps are above this threshold by *at least* a factor of 10.

However, the CMZ is 8.4 kpc away from us in the direction of our Galaxy's center, meaning there is a potentially enormous amount of material unassociated with the Sgr B2 cloud along the line of sight. This material may have column densities as low as 5×10^{21} cm^{-2} or as high as 5×10^{22} cm^{-2}, as measured from relatively blank regions in the Herschel column density map (Battersby et al. 2011). The former value corresponds to the background at high latitudes, $b \sim 0.5$, while the latter is approximately the lowest seen within our field of view. Even with the very aggressive foreground value of 5×10^{22} cm^{-2} subtracted, nearly the whole cloud exists above this threshold.

The Lada et al. (2010) sample used Spitzer observations of nearby clouds that were nearly complete to stars at least as small as 0.5 $M_\odot$. By contrast, as discussed in Section 4.1.4, our survey is sensitive only to stars with $M \gtrsim 8\ M_\odot$. The apparently higher threshold either means that there is a genuinely higher threshold for star formation in the CMZ or that there is a higher threshold for high-mass star formation that could still be universal.

REFERENCES

Barnes, A. T., Longmore, S., Battersby, C., Bally, J., & Kruijssen, J. M. D. 2016
Barnes, A. T., Longmore, S. N., Battersby, C., Bally, J., Kruijssen, J. M. D., Henshaw, J. D., & Walker, D. L. 2017, ArXiv e-prints
Battersby, C. et al. 2011, A&A, 535, A128
Caswell, J. L. et al. 2010, MNRAS, 404, 1029
Chapin, E. L., Berry, D. S., Gibb, A. G., Jenness, T., Scott, D., Tilanus, R. P. J., Economou, F., & Holland, W. S. 2013, MNRAS, 430, 2545
Clauset, A., Rohilla Shalizi, C., & Newman, M. E. J. 2007, ArXiv e-prints
Condon, J. J. & Ransom, S. 2007, Essential Radio Astronomy (NRAO)

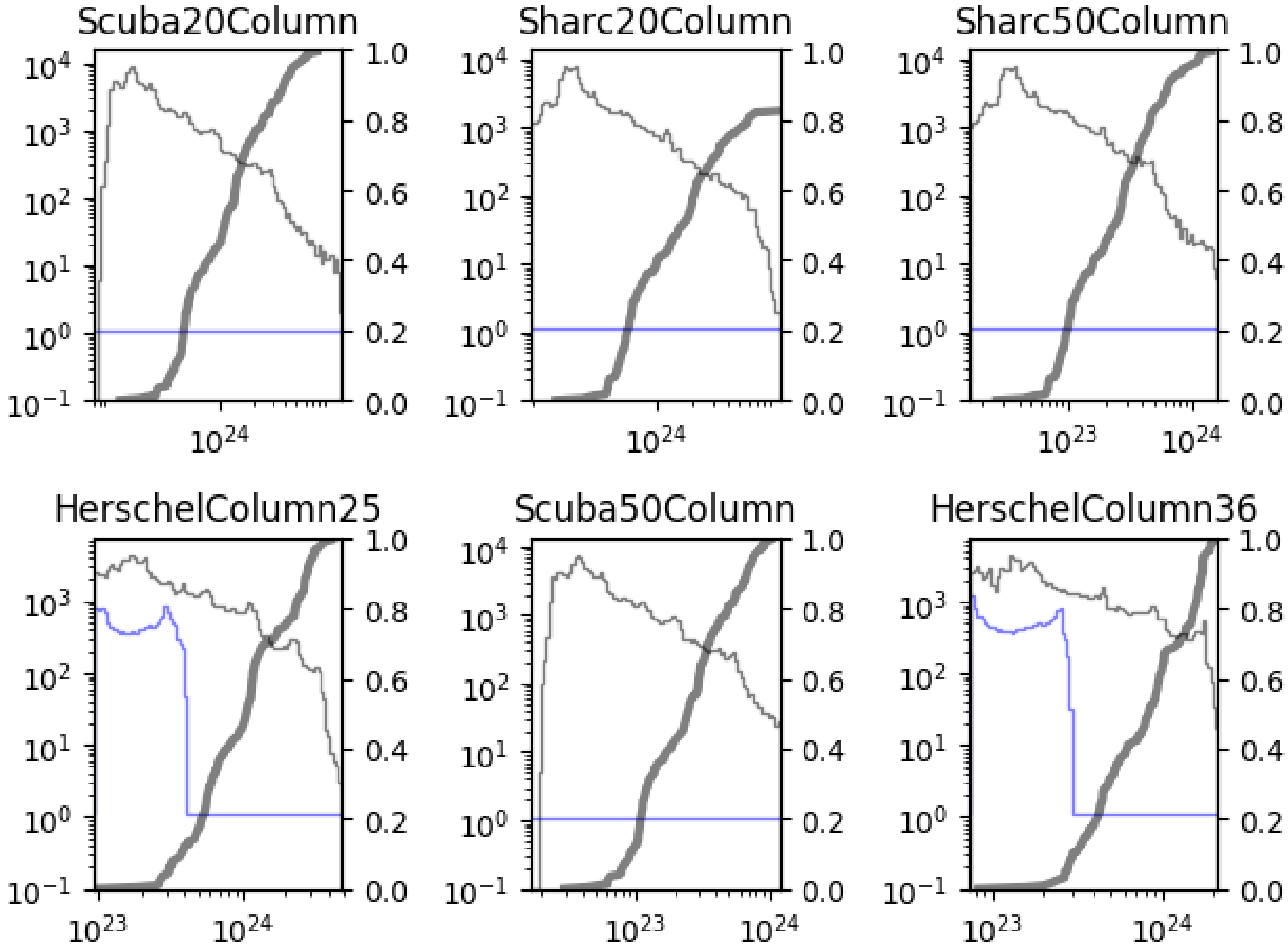

FIG. 7.— Histograms of the brightness measured with a variety of instruments at different submillimeter bands with the cumulative distribution function (CDF) of the *background* brightness surrounding each core superposed. The X-axis units are arbitrary (because right now I don't know the units of all of these) except for column, which is in units of cm^{-2} of H_2 as derived from SED fits to Herschel data (Battersby+). The grey line is of the observed region in Sgr B2 and the blue line is of G0.253+0.016. The thick grey line is the CDF of core background brightness, and is labeled by the right axis.

de Pree, C. G., Gaume, R. A., Goss, W. M., & Claussen, M. J. 1996, ApJ, 464, 788

Dicker, S. R. et al. 2009, ApJ, 705, 226

Dowell, C. D., Lis, D. C., Serabyn, E., Gardner, M., Kovacs, A., & Yamashita, S. 1999, in Astronomical Society of the Pacific Conference Series, Vol. 186, The Central Parsecs of the Galaxy, ed. H. Falcke, A. Cotera, W. J. Duschl, F. Melia, & M. J. Rieke, 453

Furlan, E. et al. 2016, ApJS, 224, 5

Gaume, R. A., Claussen, M. J., de Pree, C. G., Goss, W. M., & Mehringer, D. M. 1995, ApJ, 449, 663

Ginsburg, A. et al. 2013, ApJS, 208, 14

—. 2016, A&A, 586, A50

—. 2015, A&A, 584, L7

Henshaw, J. D. et al. 2016, MNRAS, 457, 2675

Immer, K., Kauffmann, J., Pillai, T., Ginsburg, A., & Menten, K. M. 2016, A&A, 595, A94

Johnston, K. G., Beuther, H., Linz, H., Schmiedeke, A., Ragan, S. E., & Henning, T. 2014, A&A, 568, A56

Kauffmann, J., Bertoldi, F., Bourke, T. L., Evans, II, N. J., & Lee, C. W. 2008, A&A, 487, 993

Kauffmann, J., Pillai, T., Zhang, Q., Menten, K. M., Goldsmith, P. F., Lu, X., & Guzmán, A. E. 2016a, ArXiv e-prints

Kauffmann, J., Pillai, T., Zhang, Q., Menten, K. M., Goldsmith, P. F., Lu, X., Guzmán, A. E., & Schmiedeke, A. 2016b, ArXiv e-prints

Kroupa, P. 2001, MNRAS, 322, 231

Lada, C. J., Lombardi, M., & Alves, J. F. 2010, ApJ, 724, 687

Longmore, S. N. et al. 2013, MNRAS, 433, L15

Mason, B. D., Hartkopf, W. I., Gies, D. R., Henry, T. J., & Helsel, J. W. 2009, AJ, 137, 3358

Mehringer, D. M., de Pree, C. G., Gaume, R. A., Goss, W. M., & Claussen, M. J. 1995, ApJ, 442, L29

Molinari, S. et al. 2016, ArXiv e-prints

Ossenkopf, V. & Henning, T. 1994, A&A, 291, 943

Ossenkopf-Okada, V., Csengeri, T., Schneider, N., Federrath, C., & Klessen, R. S. 2016, A&A, 590, A104

Pree, C. G. D. et al. 2015

Rathborne, J. M. et al. 2015, ApJ, 802, 125

Sahai, R., Güsten, R., & Morris, M. R. 2012a, ApJ, 761, L21

Sahai, R., Morris, M. R., & Claussen, M. J. 2012b, ApJ, 751, 69

Sanchez-Monge, A. et al. 2017

Schmiedeke, A. et al. 2016, A&A, 588, A143

Shetty, R., Beaumont, C. N., Burton, M. G., Kelly, B. C., & Klessen, R. S. 2012, MNRAS, 425, 720

Stanimirovic, S. 2002, in Astronomical Society of the Pacific Conference Series, Vol. 278, Single-Dish Radio Astronomy: Techniques and Applications, ed. S. Stanimirovic, D. Altschuler, P. Goldsmith, & C. Salter, 375–396

Yusef-Zadeh, F., Hewitt, J. W., & Cotton, W. 2004, ApJS, 155, 421

APPENDIX

SINGLE DISH COMBINATION

To measure the column density at a resolution similar to Lada et al. (2010), we needed to use ground-based single-dish data with resolution $\sim 10''$. We combined these images with Herschel data, which recover all angular scales, to fill in the missing 'short spacings' from the ground-based data.

Specifically, we combine the SHARC 350 μm (Dowell et al. 1999) and SCUBA 450 μm (**?**) with Herschel 350 and 500 μm data (Molinari et al. 2016), respectively.

Combining single-dish with 'interferometer' data, or data that are otherwise insensitive to large angular scales, is not a trivial process. The standard approach advocated by the ALMA project is to use the 'feather' process, in which two images are fourier-transformed, multiplied by a weighting function, added together, and fourier transformed back to image space (see equations in §5.2 of Stanimirovic 2002). This process is subject to substantial uncertainties, particularly in the choice of the weighting function.

Two factors need to be specified for linear combination: the beam size of the 'single-dish', or total power, image, and the largest angular scale of the 'interferometer' or filtered image. While the beam size is sometimes well-known, for single dishes operating at the top of their usable frequency range (e.g., the CSO at 350 μm or GBT at 3 mm), there are uncertainties in the beam shape and area and there are often substantial sidelobes. In interferometric data, the largest angular scale is well-defined in the originally sampled UV data, but is less well-defined in the final image because different weighting factors change the recovered largest angular scale. For ground-based filtered data, the largest recoverable angular scale is difficult to determine and requires concerted effort (e.g., Ginsburg et al. 2013; Chapin et al. 2013).

To assess the uncertainties in image combination, particularly on the brightness distribution (e.g. Ossenkopf-Okada et al. 2016), we have performed a series of experiments...

- EXPERIMENT 1: "SHARC" data with beam overestimated (real = 9, used = 12)
- EXPERIMENT 2: "SHARC" data with 50% flux calibration error
- EXPERIMENT 3: "SCUBA" data with 50% flux calibration error (extrapolation)

...With those experimental results in hand, we combined the SHARC and SCUBA images with their Herschel counterparts.